Sensitivity Analysis of Passive Intermodulation Due to Electrical Contacts

Sensitivity Analysis of Passive Intermodulation due to Electrical Contacts

Felipe Treviso, *Student Member, IEEE,* Riccardo Trinchero, *Member, IEEE,* Petri Keski-Opas, Ilkka Kelander, Flavio G. Canavero, *Fellow, IEEE.*

***Abstract*—Non-linear phenomena in electrical contacts deteriorate the quality of communication systems with the production of passive intermodulation (PIM). The theoretical evaluation of PIM as a function of the physical parameters of the contact is rather complicated. Standard linear and macroscopic contact models do not take into account all microscopic aspects of the contact responsible for its non-linear behavior. For the above reason, an accurate analysis of the PIM should be carried out by using microscopic contact models, defined by dozens of parameters, some of which cannot be precisely measured or estimated. This paper presents a statistical analysis of the PIM level by taking into account a possible uncertain interval for the physical parameters of the contact. Such statistical interpretation is then used in order to identify the most relevant physical parameters for the PIM generation via a sensitivity analysis, through the use of a surrogate model that speeds up the huge amount of PIM computations. The results of the sensitivity analysis allow to build a simpler model depending only on few dominant parameters.**

***Index Terms*—Passive intermodulation, sensitivity analysis, electrical contact, surrogate model, support vector machine.**

I. Introduction

PASSIVE intermodulation (PIM) is a form of signal distortion where spurious frequency components are produced by the non-linearity of passive elements. These spurious signals can seriously threaten the quality of communication systems, as intermodulation products may fall into the receiving band or close to carrier frequencies, making their elimination through filters difficult [1]–[3]. Therefore, a good system design must take into account the evaluation of PIM components and use strategies to reduce this type of interference.

The literature describes many possible sources of PIM [1]–[18], among which we can cite dynamic electro-thermal or electro-mechanical mechanisms, electrical discharges across micro-cracks in metals, non-linear materials (e.g. ferromagnetic) and non-linear effects across contacts. In electrical contacts, it is common to consider the tunnel effect as the most relevant non-linear effect that acts as a PIM source [3]–[6], together with the thermionic effect [7], [8]. Such effects occur at the contact interface, where highly conductive metals used in the contact might naturally form a thin film which deteriorates the conduction mechanism from one surface to another. The non-linear effects above occur at such irregular film.

An equivalent circuit is usually applied to model the electrical contact, using resistors and capacitors to account for the linear effects [2]–[5], [14], while the non-linear behavior is represented by a non-linear element described via a low-order polynomial expansion [1], [3], [4], [10]–[14], [17]. The resulting PIM is obtained from the analysis of this equivalent circuit. The tuning of the parameters required for that analysis can be either based on measured data of the contact [3], [14], or on theoretical equations that model the relation of the physical parameters of the contact and the considered phenomena [5]. Indeed, there are many physical parameters that can affect PIM generation [18], and therefore those theoretical models should be carefully assessed in order to achieve the accuracy obtained by the behavioral models. However, it is also known that it is hard to compare the PIM theory with measurements due to the difficulty in isolating the PIM sources experimentally and the reproducibility of experiments [5], [9].

Additionally, most of those parameters have an intrinsic uncertainty, as they are related to microscopic aspects of the contact, while the theoretical models take them into account as macroscopic approximations. Therefore, even if deterministic theoretical models allow to estimate the general trend of the PIM level, it is unreasonable to expect from such models to provide a deterministic and accurate prediction of the PIM level. For such reasons, PIM should be analyzed either through a statistical evaluation of the PIM level considering all the involved uncertainties, or in a more compact way, through a sensitivity analysis that will indicate which are the most relevant factors in the production of PIM. Variations of the PIM with respect to experimental parameters like carrier power and measured error have been analyzed [9], but so far there is no investigation about the sensitivity of the predictions provided by theoretical models with respect to the large number of parameters used by them (e.g., the energetic characteristics of the material, contact area and pressure, etc.). Such analysis can simplify the theoretical models by focusing only on the parameters that are most dominant for PIM generation, making its estimation simpler and speeding up its computation.

The aim of this work is a sensitivity analysis carried out via a theoretical PIM model which considers electron tunneling and thermionic emission as the non-linear mechanisms. It is based on the equivalent circuit presented in Sec. II, estimated from the physical aspects of the contact, and aims at extracting the most relevant parameters for PIM generation through a sensitivity analysis described in Sec. III. A surrogate model

This work was supported by contract YBN2020055131 sponsored by Huawei Technologies Oy (Finland) Co. Ltd.

Felipe Treviso, Riccardo Trinchero and Flavio G. Canavero are with Politecnico di Torino, Corso Duca degli Abruzzi, 24, 10129, Torino, Italy. e-mail:{felipe.treviso,riccardo.trinchero,flavio.canavero}@polito.it

Petri Keski-Opas and Ilkka Kelander are with Huawei Technologies Oy (Finland) Co. Ltd., Läkkisepäntie 23, 00620, Helsinki, Finland. e-mail: {petri.keskiopas,ilkka.kelander}@huawei.com

trained in Sec. IV is used to obtain a faster PIM evaluation such that its global sensitivity to a large number of parameters is evaluated. The results of this methodology are presented in Section V, where the PIM produced by the contact of two different metals and its sensitivity to physical parameters is quantified and a simplified model is proposed.

II. Physical-Based Model of an Electrical Contact

The electrical contact between two metallic surfaces is intricate. The usual way of describing this phenomenon is to visualize it as the contact between a flat surface and a rough surface that accounts for the roughness of both surfaces. An illustrative diagram of this interface is shown in Fig. 1, and a practical way to model them is briefly described in Appendix A. Due to microasperities present in the surfaces, the true contact area A_c where the surfaces are actually in contact to each other will be smaller than the apparent contact area A_n. The physical interface happens only where asperity peaks of the surfaces touch each other. Those contact points are called α-spots [19], [20], and a typical junction of two surfaces comprises a large number of these spots. Common materials used in electronic contacts, e.g., aluminum and nickel, will also produce a thin layer of oxide over their surface after a short exposition to the ambient air [21], and therefore when the two surfaces are put in contact to each other, they produce a metal-insulator-metal (MIM) interface. Depending on the stress produced by the contact pressure, the thin oxide layer can be ruptured, forming metal-metal (MM) contacts. There are also sections of the apparent area where the surfaces do not contact (NC) each other. All these types of interface can be observed in Fig. 1.

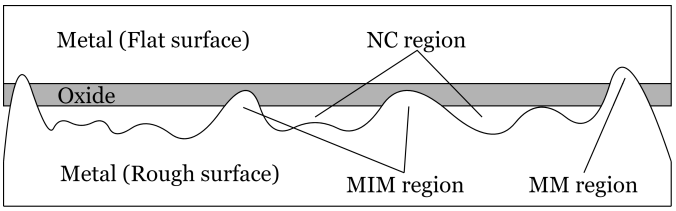

Figure 1. Illustrative diagram of the contact between a flat surface covered by an oxide layer and a clean rough surface. Regions of the three types can be identified (NC, MM, MIM, see text for explanation).

The effects on those three areas can be modeled through the equivalent circuit inside the right box in Fig. 2 [14]. The void capacitor C_n accounts for the capacitance in the NC region, where mostly air separates the conducting surfaces. In the MM region, the only circuital element is the constriction resistance R_c', which models the restriction of the current flow to the α-spots and the reduction of the volume of material used for electrical conduction due to this fact. The current in the MIM region is also constrained to flow towards the α-spots, and therefore it also observes a constriction resistance R_c'' similar to the MM region. However, the current is not able to flow freely through the α-spots because of the thin insulating oxide film. So, in series to R_c'', three elements are added to model the conduction mechanisms in this area: a film capacitance C_f, representing the effect of this thin insulator between the conducting metals, a film resistance R_f, and a non-linear conductance G_f. This non-linear element is the source of all passive intermodulation in our work, where the considered sources of non-linearity are the electron tunneling effect and the thermionic emission current through the barrier created in the MIM region [8]. The procedure to obtain each of those circuital elements is described in Appendix B. In general, an increase in the contact force favors ruptures on the film layer and increases also the contact area, bringing R_c' to very low values, and bypassing the non-linear effects of G_f, and therefore PIM is not observed on clean and tight contacts. However, according to the equations collected in the Appendices, the values and characteristics of the elements of the contact model in Fig. 2 are defined by 22 parameters, which will be listed in the next section, in order to investigate which of those parameters are the main source of PIM in loose electrical contacts.

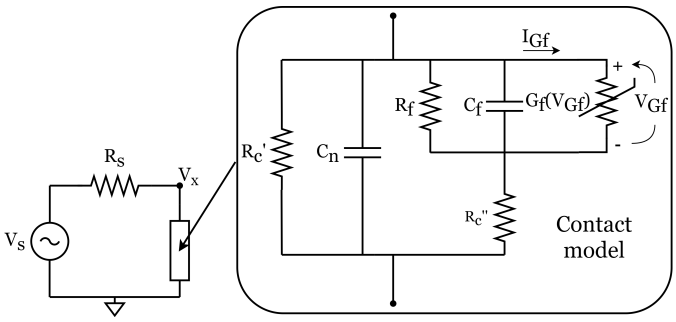

Figure 2. Circuital model of an electric contact and simulation setup simulated to evaluate the PIM produced by the contact.

In order to evaluate the PIM, the contact model is simulated in a setup that simplifies a realistic use case. It comprises a voltage source V_s with 0.45 V AC amplitude and frequency f_0= 900 MHz, in series with a resistance $R_s = 2\ \Omega$ and the contact model described above, as depicted in Fig. 2. The non-linear resistance G_f is modeled through a voltage-dependent current source which depends on its own voltage, with its current given by a polynomial with maximum order $N = 9$ which approximates the V-I curve of the considered non-linear effects according to

$$I_{Gf}(V_{Gf}) = \sum_{n=1}^{N} p_n V_{Gf}^n. \tag{1}$$

The above setup is simulated in HSPICE, where the voltage V and current I across the contact are obtained. Due to the non-linear aspect of the circuit, the simulation is a transient analysis adjusted to provide accurate frequency-domain data by applying a fast-fourier transform (FFT) on the signal waveforms with a Hamming window. The FFT is applied only to the portion of the simulation corresponding to the last 21 periods of the source V_s, to guarantee that the steady-state has been reached and avoid spurious transitory data. The procedure of setting and simulating the SPICE netlist to obtain this PIM value for one instance of the input parameters takes around 1.9 s. This work is mainly concerned with the

third intermodulation harmonics at $f = 3f_0$, i.e., V_{3f_0} for the voltage and I_{3f_0} for the current. Hereafter, when a PIM value is mentioned, it refers to the PIM power at this specific frequency in dBm, which is computed according to

$$PIM = 10\log(\Re\left\{V_{3f_0} I^*_{3f_0}/2\right\}) + 30. \quad (2)$$

III. Sensitivity Analysis

Sensitivity analysis is a technique that allows quantifying the impact of each input parameter of a system on its output. It describes how the variability of the output reacts to its combinations of input parameters [22], and by doing this, it identifies superfluous parameters that add unnecessary complexity to the model but are not essential to explain the variability of the output [22], [23]. Specifically, global sensitivity analysis methods take into account the whole input domain, while local approaches assess the impact of small perturbations of the inputs around nominal values. The global sensitivity techniques overcome the limitations of local methods, such as assumptions of linearity and normality of the system [24]. Sobol' indices are indeed one of the most advanced methods for global sensitivity analysis adopted in many state of the art papers and tools [22]–[27]. They are based on the idea of defining the expansion of the system variance into a sum of functions with inputs of increasing dimension [25]. First-order Sobol' indices S_i express the share of the output variance due to the i-th input. Interactions between parameters are taken into account by higher order indices, which account for combinations of the inputs. The total Sobol' index $S_{T,i}$ summarizes the contribution of the i-th parameter by summing all the Sobol' indices involving this parameter.

Each of these indices is traditionally evaluated through a Monte Carlo simulation, thus making their extraction unpractical with computationally expensive models or when the number of input parameters is large [22]. In order to efficiently compute the total Sobol' indices, this work uses Saltelli's algorithm [26] implemented in the Python package OpenTURNS [27]. However, a sensitivity analysis using the contact model from Sec. II with 22 input parameters is prohibitive. By considering that each Sobol' index is estimated through 100,000 PIM evaluations, 2,400,000 evaluations are required to obtain the 22 first order and total Sobol' indices [26]. Such number of computations on the proposed circuital SPICE model would require around 52 days. In order to speed up the computation, a surrogate model is built following the procedure described in the next section. This surrogate model enables a fast PIM evaluation to compute the total Sobol' indices, which provide the physical parameters with most impact in the PIM generation within the defined interval of variation.

The 22 parameters required to arrive at the contact model are shown on Table I. They consider a contact between two different metals, respectively metal 1 and metal 2, separated by a film of oxide. The sensitivity analysis also requires the definition of the range of variation of the input parameters for which the sensitivity is investigated. Such range is also indicated in Table I. Usually, contacts use highly conductive material such as, e.g. brass, aluminum, steel, which are also sometimes plated with nickel, gold, etc. Each material has its mechanical (Young modulus, Poisson ratio) and electrical properties (resistivity, work functions), as well as they might produce a different barrier in the contact (the oxide layer which they often form). All these parameters are inputs of our PIM model, so variations in the material (expressed by changes in its properties) will affect the PIM prediction. We are using as range of variation for each of the material parameters, the upper and lower bound among all the possible material combinations, in order to cover all the properties characterizing common contact materials. A similar approach is used for the other parameters. Profilometer rugosity measurements were performed in a few samples of common contact surfaces, and used to define the extremities of its variation intervals, while the other parameters such as nominal area, force, temperature were defined based on a specific contact design. The global sensitivity analysis performed will quantify how much the PIM is influenced by those parameters within these specified intervals. But first, a surrogate model is needed in order to speed up the PIM computation.

Table I
Input parameters for the model of an electric contact.

Par.	Range	Description
η	$[1\times10^4, 5\times10^4]$ [/mm^2]	Density of asperities in the surface
σ	$[0.1, 2.0]$ [μm]	Standard deviation of rugosity profile
μ	$[-30, 30]$ [nm]	Mean value of rugosity profile
R_a	$[20, 50]$ [μm]	Mean radius of the surface asperities
F	$[0.1, 0.2]$ [N]	Contact force
A_n	$4 \pm 10\%$ [cm^2]	Nominal area
T	$[25, 40]$ [C]	Contact temperature
ρ_f	$[1\times10^3, 1\times10^{12}]$ [Ωm]	Resistivity of the film
s	$[12, 60]$ [Å]	Average film thickness
ε_f	$[8, 12]$ [$-$]	Dielectric constant of film
φ_f	$[4.5, 5.2]$ [eV]	Work function of film
α	$[1, 2]$ [$-$]	Cracking effect parameter
E_g	$[2, 3]$ [eV]	Band gap of film
ρ_1	$[0.017, 0.67]$ [mΩmm]	Resistivity of metal 1
φ_1	$[4, 4.9]$ [eV]	Work function of metal 1
E_1	$[65, 200]$ [GPa]	Young modulus of metal 1
ν_1	$[0.3, 0.4]$ [$-$]	Poisson ratio of metal 1
λ_0	$[0.4, 6.5]$ [$-$]	Richardson constant correction
φ_2	$[4, 4.9]$ [eV]	Work function of metal 2
ρ_2	$[0.017, 0.67]$ [mΩmm]	Resistivity of metal 2
E_2	$[65, 200]$ [GPa]	Young modulus of metal 2
ν_2	$[0.3, 0.4]$ [$-$]	Poisson ratio of metal 2

IV. Surrogate Model for Faster PIM Evaluation

As anticipated above, a sensitivity analysis using the full theoretical-based circuital PIM model has a heavy computational cost. A surrogate model built from samples of the full simulation setup provides a simple mathematical relation between the input and output of the model from Sec. II, thus speeding up the computations. But any surrogate model requires data in order to be trained. In order to generate this data, a total of 10,972 samples are drawn in a latin hypercube sampling (LHS) of the input space from Table I, considering an uniform distribution of the specified intervals, except for ρ_f, which considered a log-uniform distribution to account for the very large variation of its interval. The uniform distribution accounts equally for any value in the interval, while the LHS draw random samples that will be guaranteed to cover in a

homogeneous way the input space [28]. For each of those samples, the output PIM level is computed according to the procedure described in Sec. II. The total simulation time for all samples takes only 5.79 hours to be performed and its result are shown in the histogram in Fig. 3.

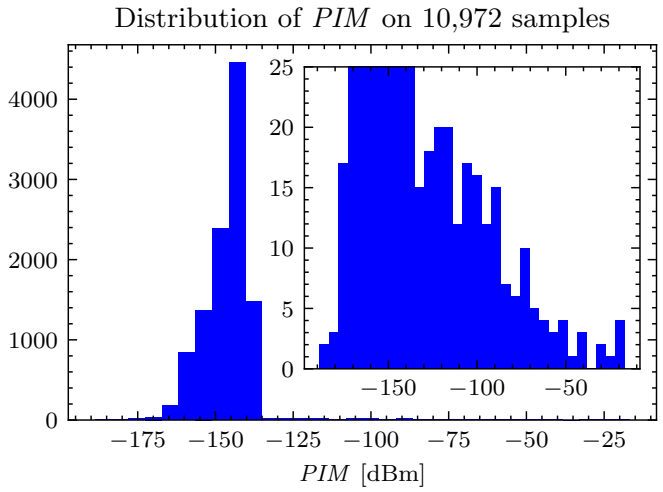

Figure 3. Distribution of PIM level from 10,972 samples.

The target surrogate model uses as input the vector $\mathbf{x}$ containing the 22 parameters from Table I, and from this input evaluates as output $PIM'(\mathbf{x})$, which is a prediction of the PIM produced with the parameters $\mathbf{x}$. The histogram of Fig. 3 shows that in most cases, the PIM level is below -140 dBm, with most samples crammed between -150 and -135 dBm. Such value is a noise limit of the simulation setup, where the numerical error becomes larger than the simulated value. On one hand, those values correspond to PIM levels that do not pose EMC issues, and thus, the focus should be on the remaining samples, where the PIM level is higher. On the other hand, such effect can compromise the accuracy of the surrogate model. Due to this fact, we define a threshold PIM_t, so that any PIM value below PIM_t is said to be negligible, and thus its exact value is not important. Considering this detail, we follow the two-step approach [29] shown in Fig. 4 when training a surrogate model to obtain an approximate output PIM': initially, the training samples are distinguished between having a relevant or irrelevant PIM values, by separating the samples above and below a threshold PIM_t with the binary label PIM_r. Then, a classification surrogate $\mathcal{C}(\mathbf{x})$ is trained for PIM_r, and only the samples classified as having a relevant PIM_r, i. e., larger than PIM_t, are passed to a regression model $\mathcal{M}(\mathbf{x})$. Such regression estimates an exact value for PIM' for all the relevant PIM samples. For the remaining, where the PIM is negligible, we set $PIM' = PIM_t$. The block highlighted in green illustrates a pre-processing of the training data made in order to add to the original data its right PIM_r label. The block in red is the actual surrogate model, trained with the data at the output of the previous block and used to predict a PIM' value for any input $\mathbf{x}$ thereafter.

The 10,972 samples are split into 70% for a training data set and 30% for a test data set. The input parameters are preprocessed by scaling them to an uniform distribution in

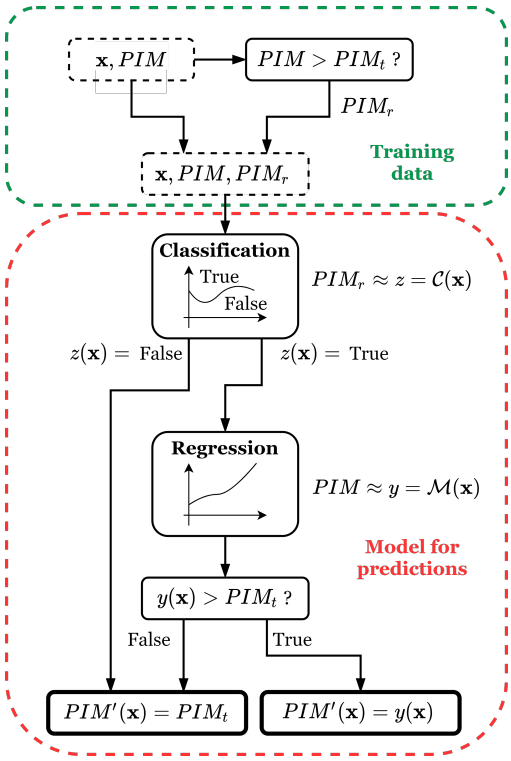

Figure 4. Structure of the surrogate model built to estimate PIM'.

the range from 0 to 1. Based in the histogram from Fig. 3, we also define the threshold $PIM_t = -135$ dBm, which is below most practical PIM limits [32], and is also able to separate the samples crowding at the numerical simulation limit. The labeled training data set is used to train a Support Vector Machine (SVM) model $z = \mathcal{C}(\mathbf{x}) \approx PIM_r$ for using a RBF kernel [30], [31]. The SVM is specially adequate for the classification task due to its property of seeking a maximum margin separation hyperplane in the input parameter space. Its detailed description, along with the formulation of the technique used for the regression model $\mathcal{M}(\mathbf{x}$ is out of the scope of this paper, but they can be found in the aforementioned references. Both techniques are implemented and optimized on Python, with functions and structures from the Scikit-learn and Scikit-optimization packages. Its hyper-parameters are optimized via a Bayesian scheme with 3-fold cross-validation and 15 optimization iterations [33]. The training is done accounting that a false negative (i.e., a relevant PIM sample is classified as irrelevant) has a cost 5 times larger than a false positive (i.e., an irrelevant PIM sample classified as relevant). The reasons for this choice are three: 1: the data is unbalanced, i.e., there are more samples with irrelevant PIM, which would have a larger weight in the final model otherwise; 2: we are more interested in the cases where electronic systems can suffer interference, which are the cases with a large PIM value; and 3: the false positives still have their value evaluated by the regression model, where they can be estimated accordingly and corrected. Then, the obtained model is used to predict PIM_r on the test data set. The confusion matrix of those predictions is shown in Fig. 5. It

shows a remarkable model accuracy when the full simulation obtains a value where PIM_r is true: out of those 61 samples, 58 were classified accordingly, an accuracy of around 95%. However, the model predicts a large absolute number of false positives: out of the 3,231 samples where PIM_r is false, 55 were misclassified as a relevant PIM sample. Despite the large number, it amounts to only 1.7% of the cases and these missclassifications produced by the model are not an issue because they still can have their right value predicted in the regression phase.

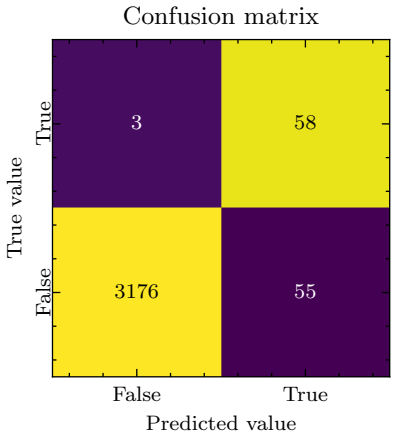

Figure 5. Confusion matrix of the model for classification of relevant PIM values applied to the validation data set.

Out of the original 10,972 samples, 330 are classified as having a relevant PIM by the validated SVM model. Only these samples are passed to the regression model $y = \mathcal{M}(\mathbf{x}) \approx PIM$, and they are now split into 90% for a training data set and 10% for a test data set. The test set is small due to limited number of samples that arrive at this branch of the model. Polynomial features up to degree 2 are added to the input parameters in order to capture higher order interactions between them, making a new input variable containing 276 dimensions. The training set is used to train a least-squares support vector machine (LS-SVM) model with a RBF kernel [31], where the hyperparameters are optimized using a 3-fold cross-validation via a Bayesian scheme with 20 iterations. Figure 6 shows the scatter plot of this LS-SVM model, providing a comparison between its predictions and the results of the full circuital simulation. It has a good performance in approximating the value of the complete model considering the large number of input parameters and high output variability, having a R^2 score equal to 0.73. The reported R^2 score refers only to the regression part of the model, i.e., the samples classified by the classification part as the ones which have $PIM > PIM_t$. Hence, it does not represent the R^2 score of the whole model, since it is computed on a small subset. Indeed, the results of the complete model will be given by the combination of the left column of Fig. 5, where 99.9% of the samples are classified correctly, plus the regression model (with R^2 score equal to 0.73) applied only to the right column of Fig. 5. The R^2 score concerns only such samples that are classified as having a relevant PIM value (3.4% of the samples in our test scenario). All samples with $PIM < PIM_t$ have their value adjusted to PIM_t. With this consideration, the total R^2 score of the surrogate model is equal to 0.82, which can be considered an acceptable value for performing the sensitivity analysis. As a further proof, the histogram in Fig. 7 provides a statistical validation of the proposed surrogate model. Specifically, it compares the PDF of the PIM predicted by the regression part of the proposed surrogate model with the one computed from the circuital simulations (which are used as reference). The plots highlight the capability of the proposed model to accurately predict the actual behavior of the PIM level. It is important to remark, that without this unusual two-step procedure, it would have been impossible to achieve the model accuracy reported in this work, as the very high number of samples with -150 dBm< PIM <-135 dBm (more than 95% of all samples) would force the model to produced outputs in that range.

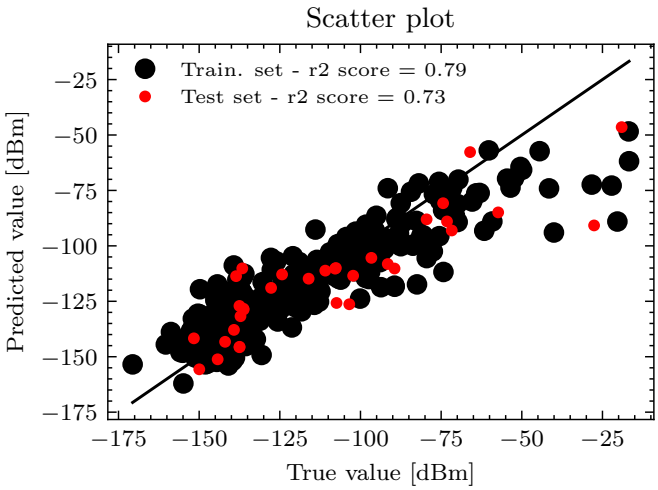

Figure 6. Scatter plot of the PIM level with a comparison between the true value and the LS-SVM model prediction for the samples with relevant PIM.

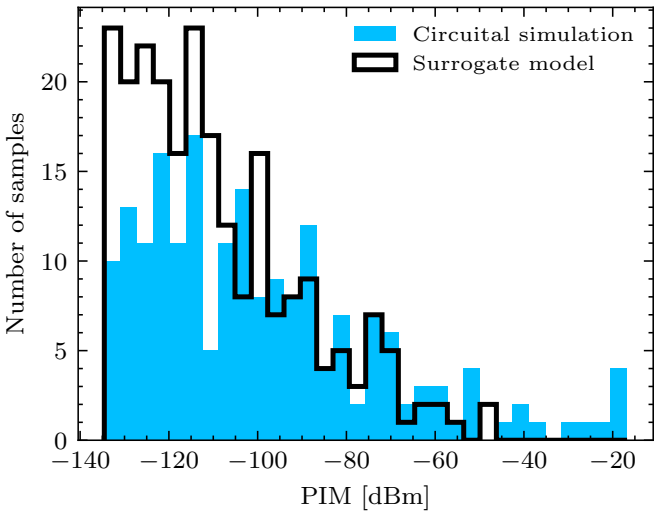

Figure 7. Distribution of PIM level on the samples classified with $PIM > PIM_t$.

V. Sensitivity Analysis' Results

A. PIM Sensitivity with Respect to Input Parameters

The first order and total Sobol' indexes described in Sec. for all the 22 parameters III are predicted by means of the surrogate model for PIM' shown in Fig. 4. By using this surrogate model, the total time is reduced from 52 days to 5.92 minutes, with little loss of accuracy. Figure 8 shows the magnitude of the Sobol' indexes for all the inputs of our model.

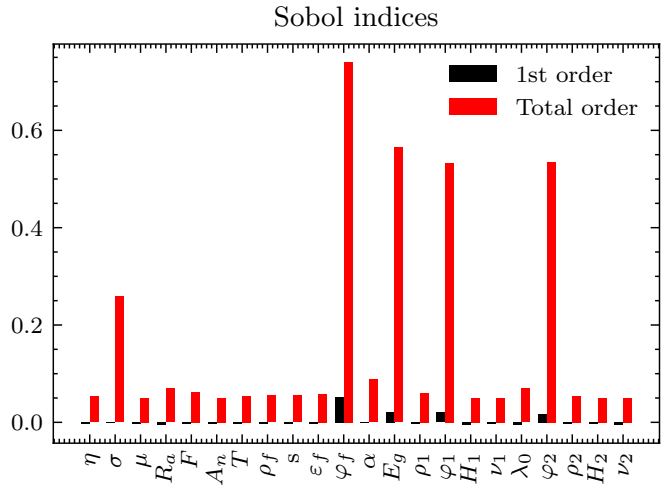

Figure 8. Total Sobol' indexes obtained for the input parameters and variability in Table I.

All the first order Sobol' indexes obtained in the analysis had a negligible value. This fact means that the variation of a single parameter within the indicated intervals is not able to explain the observed PIM level variations, i.e., no parameter is able to explain PIM production alone. However, the total Sobol' indexes indicate the total cumulative importance of each parameter in the output. Among the 22 parameters considered in the analysis, with the variability interval employed there, the total Sobol' indices show that the PIM level behavior is dominated by 5 parameters: the work function of the film; the bandgap of the film; the work functions of the metals; and the standard deviation of the surface roughness profile. All other inputs present a small contribution to the PIM level in the analyzed model, yet one should keep in mind that they might be relevant if the conditions are changed (e.g., if V_s has a larger value or if parameters have a more restrict range of variation), and thus should not be completely discarded in other models. Additionally, the four most relevant parameters are related to the involved material, where the possible design choices are limited by the available options, thus the designer might need to act also on the other parameters to mitigate the PIM.

Nonetheless, we are able to provide a general trend of the PIM variation as function of those most important input parameters, and this can be done by observing the distribution of parameters that produced a PIM larger than PIM_t. Those distributions are shown in Fig. 9. Out of the original uniformly distributed parameters, a relevant PIM level clearly tends to appear mostly for small values of the metal work functions φ_1 and φ_2, small values of the bandgap E_g, and high values for the film work function φ_f and roughness profile standard deviation σ. Although the nominal contact area did not appear in the list of most relevant parameters of the analysis, it is strongly influenced by σ. Such parameter is used to compute the standard deviation of the height of asperity peaks σ_s and strongly influences the true contact area A_c.

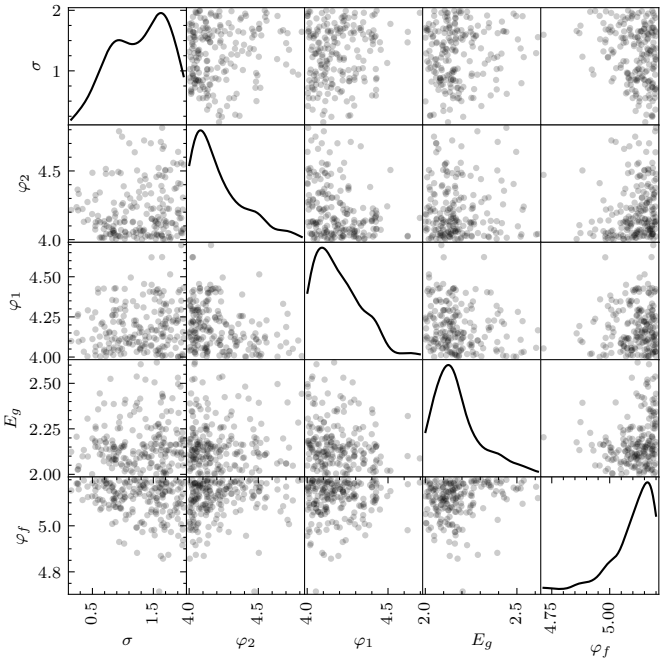

Figure 9. Distribution of the input parameters that generated a PIM level larger than PIM_t.

B. Construction of Simplified Models from the Sensitivity Analysis

We can exploit the sensitivity analysis of PIM carried out in Sect. V-A in order to reduce the number of input parameters required to predict PIM' [34]. The Sobol' indices in Fig. 8 show that most of the variance in the PIM is explained by only 5 parameters: φ_1, φ_2, φ_f, E_g and σ. This indicates that the energy barrier in the insulator is the main responsible for the PIM production, together with σ, which seems to be the parameter with most influence in the contact area determination. Therefore, we propose to observe the PIM production considering only such parameters as input. We replace the classification model $\mathcal{C}(\mathbf{x})$ by a reduced model $\mathcal{C}^r(\mathbf{x}^r)$, and the regression model $\mathcal{M}(\mathbf{x})$ by $\mathcal{M}^r(\mathbf{x}^r)$, which are trained by taking as input only the reduced vector of parameters $\mathbf{x}^r = [\varphi_1, \varphi_2, \varphi_f, E_g, \sigma]^T$. By following the same procedure from Sec. IV, we can achieve a good surrogate model which takes as input $\mathbf{x}^r$. The confusion matrix of $\mathcal{C}^r(\mathbf{x}^r)$ is shown in Fig. 10, and the scatter plot of $\mathcal{M}^r(\mathbf{x}^r)$ is shown in Fig. 11. These two figures show that a similar accuracy performance can be obtained through the simplified model, thus validating the results of the sensitivity analysis via the Sobol' indices. They also show that the most relevant

parameters are able to predict the PIM in this system with an acceptable accuracy, which could provide a more efficient tool if other design characteristics of the PIM system would be analyzed, e.g., the variability of some design target.

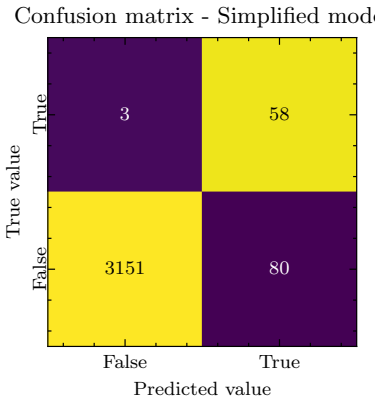

Figure 10. Confusion matrix of the simplified model for classification of relevant *PIM* values applied to the validation data set.

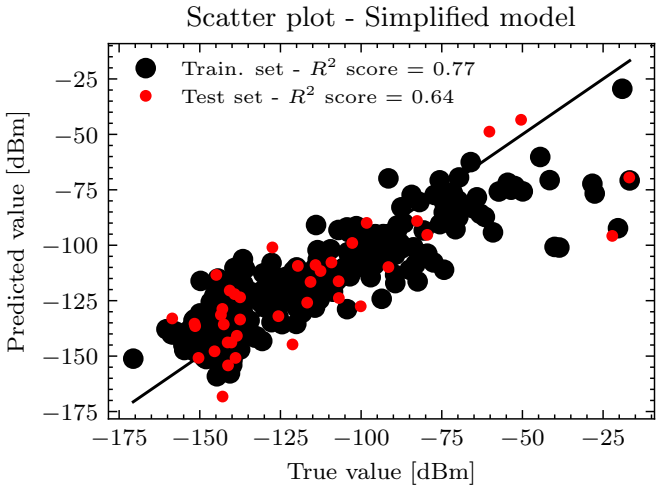

Figure 11. Scatter plot of the *PIM* level with a comparison between the true value and the LS-SVM simplified model prediction for the samples with relevant *PIM*.

VI. Conclusion

The methodological application of current theory for the modelling of electrical contacts allowed us to obtain a model based on physical input parameters for the contact behavior. The simulation of that model provides us the *PIM* level for a certain combination of parameters. Our surrogate model obtained from a few samples of the theoretical model provides an accurate way to evaluate the *PIM* level without requiring the estimation of the contact model and its simulation, and thus it is much faster to evaluate: since a sensitivity analysis via Sobol' indices considering 22 parameters requires millions of samples, such high number of simulations in the circuital model would take around 52 days. In comparison, the trained surrogate model can obtain those samples in only 5.92 minutes (and up to 6 hours simulating the circuital model to generate the training samples), enabling a sensitivity analysis of the PIM with respect to all the input parameters.

The sensitivity analysis indicates that the most important parameters for the *PIM* level are the work function of the film, the bandgap of the film, the work functions of the metals, and the standard deviation of the surface roughness profile. A simplified model taking as input only these 5 most relevant parameters provided a rough prediction of the PIM level, validating the the sensitivity analysis. The above analysis allows to identify a small set of physical parameters which mostly affect the PIM. The obtained results can be used by the EMC designer as a direction to be focused to minimize the PIM level, when designing a problematic PIM contact. The results of this work showed that a focus in material selection and in the rugosity of the surface will have the most impact in the PIM.

Appendix A
Analytical Model of the True Contact Area

Considering that the contact of the surfaces in Fig 1 is given by elastic deformation, it is commonly treated through the Greenwood-Williamson model. This statistical model depends on the topography of the surface and the statistical distribution of asperities [21], [35], [36]. Its theoretical details can be found in the literature, but a practical implementation can start with the computation of an equivalent Young's modulus [5], [37] $E_\prime$:

$$E' = \left(\frac{1-\nu_1^2}{E_1} + \frac{1-\nu_2^2}{E_2} \right)^{-1}, \tag{3}$$

where E_1, E_2, ν_1 and ν_2 are the Young's modulus and Poisson ratio of the two involved materials. Additionally, from the the surface roughness profile, a roughness parameter β is computed according to $\beta = \eta \sigma R_a$, where η is the density of asperities, σ is the standard deviation of the roughness profile and R_a is the mean radius of the surface asperities. This parameter β is used to estimate the standard deviation of the asperity heights σ_s through $\sigma_s = \sigma\sqrt{1 - 3.717 \cdot 10^{-4}/\beta^2}$ [5]. These are fundamental parameters to the Greenwood-Williamson model. Another fundamental equation is the integral

$$F_n(x) = \frac{1}{\sqrt{2\pi}} \int_x^\infty (t-x)^n e^{-t^2/2} dt, \tag{4}$$

which appears in different instances of the model with $n =$ 0, 1 and 3/2 [37].

Based on the total load supported by the asperities F (in N), we can estimate the distance d from the summit mean plane to the contact point between the surfaces as the argument of

$$F_{3/2}(d/\sigma_s) = \frac{3F}{4A_n E' R_a^{1/2} \sigma_s^{3/2} \eta}. \tag{5}$$

Having encountered d/σ_s, the number of contact spots N_c can also be estimated as [5]

$$N_c = \eta A_n F_0(d/\sigma_s). \tag{6}$$

Another important parameter is the average deformation distance of each microasperity $\bar{l}$ [5], which is computed as

$\bar{l} = F_1(d/\sigma_s)$. Finally, the contact area is estimated from the previous parameters as [37]

$$A_c = A_n \pi R_a \sigma_s \eta \bar{l}. \tag{7}$$

Originally, the surface was covered with a thin oxide layer. The cracking of this layer to form MM contacts is not fully understood and modeled yet, although Vicente postulates an expression to take into account such phenomenon [5] and split A_c into MM and MIM contact areas, respectively A_{MM} and A_{MIM}. Intuitively, the film is more likely to rupture when the applied contact pressure is larger, and when the original film was thinner [5]. Therefore, it was postulated that this effect is modeled through

$$A_{MM} = A_c \left(\frac{\bar{l}/s}{1 + \bar{l}/s} \right)^{\alpha}, \tag{8}$$

where $\alpha > 0$ is a tunable parameter that models how the MM region grows with the increase of the force. Evidently, the contact area plus the area of the NC region A_{nc} compose the apparent contact area according to

$$A_n = A_c + A_{nc} = A_{MM} + A_{MIM} + A_{nc}. \tag{9}$$

Appendix B
Computation of the Circuital Elements of the Contact Model

Regarding the circuit in (2), the void capacitor C_n in the NC region is computed according to [14]

$$C_n = \frac{\varepsilon_0 A_{nc}}{d}, \tag{10}$$

where ε_0 is the dielectric constant of the vacuum.

In the contact region, the constriction resistance R_c' is computed according to [19], [20]

$$R_c' = \frac{\rho_1 + \rho_2}{4a} = \frac{\rho_1 + \rho_2}{4N_c} \sqrt{\frac{N_c \pi}{A_{MM}}}, \tag{11}$$

where ρ_1 and ρ_2 are the resistivity of the two contacting metals, η is an empirical coefficient of order unity and a is the Holm's radius, a radius that defines a fictitious circular contact area where the current is constrained to flow through uniformly [20], and that is based on the true contact area. Similarly, the constriction resistance in the MIM region R_c'' follows the same logic, but this time related to A_{MIM}:

$$R_c'' = \frac{\rho_1 + \rho_2}{4N_c} \sqrt{\frac{N_c \pi}{A_{MIM}}}. \tag{12}$$

In series to R_c'', the film capacitance C_f and a film resistance R_f are computed as

$$C_f = \frac{\varepsilon_f \varepsilon_0 A_{MIM}}{s}, \tag{13}$$

and

$$R_f = \frac{s\, \rho_f}{A_{MIM}}, \tag{14}$$

where s is the average film thickness, ε_f is the dielectric constant of the oxide film and ρ_f is the film resistivity.

In order to model the non-linear effects of G_f, let us consider the generic case of two metallic electrodes, each with its own work function φ_1 and φ_2, that are separated by a thin film with electron affinity χ. This insulating film creates a potential barrier that interrupts the flow of electrons, as shown in Fig. 12. Electronic current can pass through this region if they have enough thermal energy to surmount the potential barrier and flow into the conduction band or if the barrier is thin enough to be penetrated by the tunnel effect when a voltage V is applied [38], [39]. The tunnel current density J_{tn} is computed according to (15) [40], where s is given in Å, $\Delta_\varphi = \varphi_1 - \varphi_2$, $\bar{\varphi} = (\varphi_1 + \varphi_2)/2$ and χ can be approximated based on the work function of the insulating film φ_f and its band gap E_g through $\chi = \varphi_f - E_g/2$.

On the other hand, the thermal emission current density J_{th} through the same barrier depends also on the temperature T (in K), and is modeled through [8]

$$\begin{aligned} J_{th} = \quad & A^* T^2 \exp\left(-\tfrac{q\bar{\varphi}}{k_0 T}\right) \\ & \exp\left(\tfrac{1}{k_0 T}\sqrt{\tfrac{q^3 V}{4\pi\varepsilon_f \varepsilon_0 s}}\right)\left[1 - \exp\left(-\tfrac{qV}{k_0 T}\right)\right], \end{aligned} \tag{16}$$

where the Boltzman constant k_0 =1324 eV/K, and A^* is the effective Richardson constant. The effective Richardson constant can be represented as $A^* = \lambda_0 A_0$, where λ_0 is a material specific coefficient and A_0 = 1.20173 $\times 10^6$ A/(m^{2}K^2). It can also be estimated [41] from the effective mass m^* and charge q_e of the electrons as

$$A^* = \frac{4\pi m^* k^2 q_e}{h^3}. \tag{17}$$

By making the correction factor that considers the effective mass of the electrons $\lambda_0 = m^*/m_e$, the effective Richardson constant is computed and used in the estimation of J_{th}.

After computing J_{tn} and J_{th}, the non-linear current I_{Gf} is given by

$$I_{Gf} = (J_{tn} + J_{th})\, A_{MIM}. \tag{18}$$

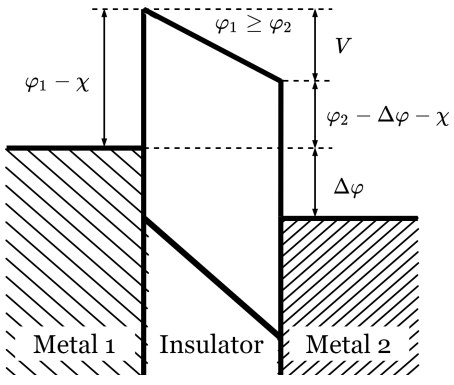

Figure 12. Illustration of a rectangular barrier between two different metals.

References

[1] Lui, P.L. "Passive intermodulation interference in communication systems," Electronics & Communication Engineering Journal, 1990, 2, (3), p. 109-118.

[2] H. Yang, H. Wen, Y. Qi and J. Fan, "An Equivalent Circuit Model to Analyze Passive Intermodulation of Loose Contact Coaxial Connectors," in IEEE Transactions on Electromagnetic Compatibility, vol. 60, no. 5, pp. 1180-1189, Oct. 2018, doi: 10.1109/TEMC.2018.2794992.

$$J_{tn}=\begin{cases}\frac{6.4\cdot10^{10}}{s}\left\{\exp\left[-1.06s\sqrt{\bar{\varphi}-\chi}\right]\right\}\left[0.53V\sqrt{\bar{\varphi}-\chi}+\frac{\left(6.3\cdot10^{4}s^{2}V^{3}\right)}{\sqrt{\bar{\varphi}-\chi}}\right], & V\leq\frac{\sqrt{\bar{\varphi}-\chi}}{2s}\\ \frac{6.4\cdot10^{10}}{s}\left\{\left(\bar{\varphi}-\chi-\frac{V}{2}\right)\exp\left[-1.06\sqrt{\bar{\varphi}-\chi-\frac{V}{2}}\right]\left(\bar{\varphi}-\chi+\frac{V}{2}\right)\exp\left[-1.06\sqrt{\bar{\varphi}-\chi+\frac{V}{2}}\right]\right\}, & \frac{\sqrt{\bar{\varphi}-\chi}}{2s}<V\leq\frac{15\sqrt{\bar{\varphi}-\chi}}{s}\\ \frac{6.4\cdot10^{10}}{s}\left(\bar{\varphi}-\chi-\frac{V}{2}\right)\exp\left[-1.06\sqrt{\bar{\varphi}-\chi-\frac{V}{2}}\right] & \frac{15\sqrt{\bar{\varphi}-\chi}}{s}<V\leq\varphi_2-\chi\\ \frac{2.4\cdot10^{10}}{s}\quad\left\{\left[\left(V+\Delta_\varphi\right)^{\frac{1}{2}}\left[V-\left(\varphi_2-\chi\right)\right]+\frac{1.33}{s}\left(V+\Delta_\varphi\right)\right]\exp\left[-1.06s\left(\frac{V+\Delta_\varphi}{2}\right)^{\frac{1}{2}}\right]+\right.\\ \quad+\frac{1}{1.50s}\frac{\left(V+\Delta_\varphi\right)^{2}}{\varphi_1-\chi}\exp\left[-0.706s\frac{\left(\varphi_1-\chi\right)^{\frac{3}{2}}}{V+\Delta_\varphi}\right]+ & \varphi_2-\chi<V\leq\varphi_2-\chi+\frac{10}{s}\\ \quad\left.-\,0.707\left[\left[V-\left(\varphi_2-\chi\right)\right]\left(V+\Delta_\varphi\right)^{\frac{1}{2}}+\frac{V+\Delta_\varphi+\varphi_1-\chi}{2.12s}\right]\exp\left[-0.706s\left(V+\Delta_\varphi\right)^{\frac{1}{2}}\right]\right\},\\ \frac{1.6\cdot10^{10}}{s}\frac{\left(V+\Delta_\varphi\right)^{2}}{\varphi_1-\chi}\left\{\exp\left[-0.706s\frac{\left(\varphi_1-\chi\right)^{3/2}}{V+\Delta_\varphi}\right]\right\}, & V>\varphi_2-\chi+\frac{10}{s}\end{cases}\tag{15}$$

[3] Li, T., Zhang, K., Jiang, J. et al. Passive intermodulation analysis of single contact junctions of wire mesh. J Comput Electron 17, 101–109 (2018).

[4] J. Russer, A. Ramachandran, A. Cangellaris and P. Russer, "Phenomenological Modeling of Passive Intermodulation (PIM) due to Electron Tunneling at Metallic Contacts," 2006 IEEE MTT-S International Microwave Symposium Digest, San Francisco, CA, 2006, pp. 1129-1132.

[5] C. Vicente and H. L. Hartnagel, "Passive-intermodulation analysis between rough rectangular waveguide flanges," in IEEE Transactions on Microwave Theory and Techniques, vol. 53, no. 8, pp. 2515-2525, Aug. 2005.

[6] W. H. Higa, "Spurious signals generated by electron tunneling on large reflector antennas," in Proceedings of the IEEE, vol. 63, no. 2, pp. 306-313, Feb. 1975.

[7] S. Zhang, X. Zhao, F. Gao and Y. He, "Study of Metal Contact Resistance and its Statistical Correlationship with Passive Intermodulation," 2018 IEEE Holm Conference on Electrical Contacts, Albuquerque, NM, 2018, pp. 353-358.

[8] S. Zhang, X. Zhao, Z. Cao, K. Zhang, F. Gao and Y. He, "Experimental Study of Electrical Contact Nonlinearity and its Passive Intermodulation Effect," in IEEE Transactions on Components, Packaging and Manufacturing Technology, vol. 10, no. 3, pp. 424-434, March 2020.

[9] L. Zhang et al., "A Composite Exponential Model to Characterize Nonlinearity Causing Passive Intermodulation Interference," in IEEE Transactions on Electromagnetic Compatibility, vol. 61, no. 2, pp. 590-594, April 2019.

[10] D. S. Kozlov, A. P. Shitvov and A. G. Schuchinsky, "Polynomial model for high-order and multi-carrier passive intermodulation products," 2016 46th European Microwave Conference (EuMC), London, 2016, pp. 631-634.

[11] He Huan and Fu Wen-bin, "On passive intermodulation at microwave frequencies," Asia-Pacific Conference on Environmental Electromagnetics, 2003. CEEM 2003. Proceedings., Hangzhou, China, 2003, pp. 422-425.

[12] L. Zhang, H. Wang, S. He, H. Wei, Y. Li and C. Liu, "A Segmented Polynomial Model to Evaluate Passive Intermodulation Products From Low-Order PIM Measurements," in IEEE Microwave and Wireless Components Letters, vol. 29, no. 1, pp. 14-16, Jan. 2019.

[13] X. Zhao et al., "Analytic Passive Intermodulation Model for Flange Connection Based on Metallic Contact Nonlinearity Approximation," in IEEE Transactions on Microwave Theory and Techniques, vol. 65, no. 7, pp. 2279-2287, July 2017.

[14] Q. Jin, J. Gao, G. T. Flowers, Y. Wu and G. Xie, "Modeling of Passive Intermodulation With Electrical Contacts in Coaxial Connectors," in IEEE Transactions on Microwave Theory and Techniques, vol. 66, no. 9, pp. 4007-4016, Sept. 2018.

[15] Arazm, Farrokh and F. Benson. "Nonlinearities in Metal Contacts at Microwave Frequencies," IEEE Transactions on Electromagnetic Compatibility EMC-22 (1980): 142-149.

[16] J. R. Wilkerson, "Passive Intermodulation Distortion in Radio Frequency Communication Systems," Ph.D. dissertation, Grad. Faculty of North Carolina State Univ., Raleigh, NC, 2010. Accessed on: Nov 12, 2020. [Online]. Available: https://people.engr.ncsu.edu/mbs/Publications/vitae_theses/wilkerson_phd_2010.pdf

[17] X. Chen et al., "Analytic Passive Intermodulation Behavior on the Coaxial Connector Using Monte Carlo Approximation," in IEEE Transactions on Electromagnetic Compatibility, vol. 60, no. 5, pp. 1207-1214, Oct. 2018, doi: 10.1109/TEMC.2018.2809449.

[18] X. Chen, L. Wang, S. Yang and M. Yu, "Empirical Passive Intermodulation Multiphysics Modeling Using Design of Experiment Method," in IEEE Transactions on Instrumentation and Measurement, vol. 69, no. 12, pp. 9371-9373, Dec. 2020, doi: 10.1109/TIM.2020.3031839.

[19] R. S. Timsit, "Electrical contact resistance: properties of stationary interfaces," in IEEE Transactions on Components and Packaging Technologies, vol. 22, no. 1, pp. 85-98, March 1999.

[20] R. Holm, Electric Contacts: Theory and Application, 4th Edition. Springer-Verlag Berlin Beideiberg, New York: 1967.

[21] M. Braunovic, V. V. Konchits, N. K. Myshkin, Electrical Contacts: Fundamentals, Applications and Technologies. CRC Press, Boca Raton, FL: 2007.

[22] S. Marelli, C. Lamas, K. Konakli, C. Mylonas, P. Wiederkehr, B. Sudret, UQLab user manual - Sensitivity analysis, Report # UQLAB-V1.3-106, Chair of Risk, Safety and Uncertainty Quantification, ETH Zurich, Switzerland, 2019.

[23] M. Larbi, I. S. Stievano, F. G. Canavero and P. Besnier, "Variability Impact of Many Design Parameters: The Case of a Realistic Electronic Link," in IEEE Transactions on Electromagnetic Compatibility, vol. 60, no. 1, pp. 34-41, Feb. 2018.

[24] Iooss B., Lemaître P. (2015) A Review on Global Sensitivity Analysis Methods. In: Dellino G., Meloni C. (eds) Uncertainty Management in Simulation-Optimization of Complex Systems. Operations Research/Computer Science Interfaces Series, vol 59. Springer, Boston, MA.

[25] I.M Sobol, "Global sensitivity indices for nonlinear mathematical models and their Monte Carlo estimates," Mathematics and Computers in Simulation, Volume 55, Issues 1–3, 2001, pp. 271-280.

[26] Saltelli, A. Making best use of model evaluations to compute sensitivity indices. Computer Physics Communication, 2002, 145, 580-297.

[27] Baudin M., Dutfoy A., Iooss B., Popelin AL. (2017) OpenTURNS: An Industrial Software for Uncertainty Quantification in Simulation. In: Ghanem R., Higdon D., Owhadi H. (eds) Handbook of Uncertainty Quantification. Springer, Cham.

[28] M. McKay, R. Beckman and W. Conover, "A comparison of three methods for selecting values of input variables in the analysis of output from a computer code", *Technometrics*, vol. 42, no. 1, pp. 55–61, 2000.

[29] H. Ma, E. Li, A. C. Cangellaris and X. Chen, "Support Vector Regression-Based Active Subspace (SVR-AS) Modeling of High-Speed Links for Fast and Accurate Sensitivity Analysis," in IEEE Access, vol. 8, pp. 74339-74348, 2020.

[30] R. Trinchero, M. Larbi, H. M. Torun, F. G. Canavero and M. Swaminathan, "Machine Learning and Uncertainty Quantification for Surrogate Models of Integrated Devices With a Large Number of Parameters," in IEEE Access, vol. 7, pp. 4056-4066, 2019.

[31] J.A.K. Suykens *et al.*, "Least Squares Support Vector Machines", World Scientific, Singapore, 2002 (ISBN 981-238-151-1).

[32] Anritsu Company (2014). Understanding PIM (Application Note 11410-00629F). Retrieved from Anritsu website: https://dl.cdn-anritsu.com/en-us/test-measurement/files/Application-Notes/Application-Note/11410-00629F.pdf

[33] Dewancker, Ian, et al. "Bayesian Optimization for Machine Learning: A Practical Guidebook." ArXiv:1612.04858 [Cs], Dec. 2016. arXiv.org, http://arxiv.org/abs/1612.04858.

[34] M. Larbi, I. S. Stievano, F. G. Canavero and P. Besnier, "Crosstalk analysis of printed circuits with many uncertain parameters using sparse polynomial chaos metamodels," 2017 International Symposium on Electromagnetic Compatibility - EMC EUROPE, 2017, pp. 1-6.

[35] Greenwood J. A. and Williamson J. B. P. "Contact of nominally flat surfaces," in Proc. R. Soc. Lond. A295300–319, 1966.
[36] P. G. Slade, Electrical Contacts: Principles and Applications, 2nd Edition. CRC Press, Boca Raton, FL: 2014.
[37] John I. McCool, "Comparison of models for the contact of rough surfaces," in Wear, Volume 107, Issue 1, 1986, pp. 37-60.
[38] C. D. Bond, C. S. Guenzer and C. A. Carosella, "Intermodulation generation by electron tunneling through aluminum-oxide films," in Proceedings of the IEEE, vol. 67, no. 12, pp. 1643-1652, Dec. 1979.
[39] John G. Simmons, "Generalized Formula for the Electric Tunnel Effect between Similar Electrodes Separated by a Thin Insulating Film," Journal of Applied Physics 34:6, 1793-1803, 1963.
[40] Forlani, F., Minnaja, N. "Rectification by means of metal-dielectric-metal sandwiches," Nuovo Cim 31, 1246–1257, 1964.
[41] Nicholls, J., Dimitrijev, S., Tanner, P. et al., "Description and Verification of the Fundamental Current Mechanisms in Silicon Carbide Schottky Barrier Diodes," Sci Rep 9, 3754, 2019.

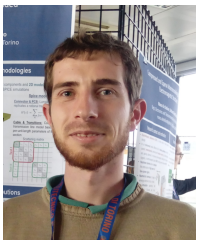

Felipe Treviso receveid his bachelor and master degrees in Electrical Engineering from Universidade Federal do Rio Grande do Sul, Porto Alegre, Brazil, in 2014 and 2016, respectively. Since 2018, he is a PhD candidate at the electronics department of Politecnico di Torino, Torino, Italy, working on the modeling of electrical interconnections. He received the Best Student Paper Award at the 25th IEEE Workshop on Signal and Power Integrity and an honorable mention in the URSI Student Paper Competition at the URSI General Assembly and Scientific Symposium 2020.

Riccardo Trinchero (M'16) received the M.Sc. and the Ph.D. degrees in Electronics and Communication Engineering from Politecnico di Torino, Torino, Italy, in 2011 and 2015, respectively. He is currently aa Assistant Professor within the EMC Group with the Department of Electronics and Telecommunications at the Politecnico di Torino. His research interests include the analysis of linear time-varying systems, modeling and simulation of switching converters and statistical simulation of circuits and systems.

Petri Keski-Opas received M.Sc. degree in electrical engineering from Tampere University of Technology, Finland, in 2001. From year 2000, he has held several electromagnetic compatibility design and simulation engineer positions in Nokia, Microsoft and currently in Huawei Technologies. His expertise also covers low frequency electromagnetic actuator simulations and design and static magnetic designs. Several product program level EMC/ESD type approval responsibilities with strong experience in problem solving and product quality improvements.

Ilkka Kelander received the M.Sc. degree in electrical engineering from the Helsinki University of Technology, Finland, in 2001. Since 2000, he has been working in Nokia, Microsoft and currently in Huawei Technologies, in Helsinki, concentrating on mobile phone electromagnetic simulation methodology research and development, including antennas, EMC and transmission line modeling. During his career, he has done product related electromagnetic design optimization and also participated in several research projects in the EMC area.

Flavio G. Canavero (SM'99-F'07-LF'22) received his electronic engineering degree from Politecnico (Technical University) of Torino, Italy, and the PhD degree from the Georgia Institute of Technology, Atlanta, USA, in 1986. Currently he is a Professor of Circuit Theory with the Department of Electronics and Telecommunications, Politecnico di Torino. He is an IEEE Fellow. He has been the Editor-in-Chief of IEEE Transactions on Electromagnetic Compatibility, V.P. for Communication Services of the EMC Society and Chair of URSI Commission E. He received several Industry and IEEE Awards, including the prestigious Richard R. Stoddard Award for Outstanding Performance, which is the EMC Society's highest technical award, and the Honored Member Award of EMC Society. His research interests include signal integrity and EMC design issues, interconnect modeling, black-box characterization of digital integrated circuits, EMI and statistics in EMC.